

Collisionality and magnetic geometry effects
on tokamak edge turbulent transport:
I. A two-region model with application to blobs

J. R. Myra, D.A. Russell and D. A. D'Ippolito

Lodestar Research Corp., 2400 Central Ave. P-5, Boulder, Colorado 80301

June 2006 (revised September 2006)
submitted to Phys. Plasmas

DOE/ER/54392-36

LRC-06-111

LODESTAR RESEARCH CORPORATION
2400 Central Avenue
Boulder, Colorado 80301

Collisionality and magnetic geometry effects on tokamak edge turbulent transport:

I. A two-region model with application to blobs

J. R. Myra, D.A. Russell and D. A. D'Ippolito

Lodestar Research Corp., 2400 Central Ave. P-5, Boulder, Colorado 80301

Abstract

A two-region model is proposed to study the effect of collisionality and magnetic geometry on electrostatic turbulence and on the propagation of filamentary coherent structures (blobs) in the edge and scrape-off-layer. The model invokes coupled vorticity and continuity equations in two different spatial regions along the magnetic field, taking into account the effect of magnetic field fanning and shear, e.g. near magnetic X-points. A linear dispersion relation for unstable modes illustrates the physics of mode disconnection (ballooning) along the magnetic field and its dependence on collisionality and wavenumber (scale size). Employing an invariant scaling analysis, dimensionless parameters for the nonlinear model are developed and used to describe the regimes of the system. A blob correspondence rule is postulated to relate the linear mode growth rates and regimes to the convective velocity of blobs. Nonlinear numerical simulations of blob convection show good agreement with a blob dispersion relation derived from the correspondence rule. It is found that collisionality increases the convective velocity. The convective velocity also depends on blob scale size, with either positive or negative exponent, depending on the collisionality regime. Finally, the dimensionless scaling analysis is employed to obtain bounds on the convective velocity suitable for experimental tests.

PACS: 52.35.Ra, 52.25.Fi, 52.40.Hf, 52.55.Fa, 52.65.-y

I. Introduction

For magnetic confinement devices, turbulent transport from the edge plasma (i.e. the steep gradient region inside the magnetic separatrix) into and across the scrape-off-layer (SOL) (i.e. the region outside the separatrix where field lines connect to material surfaces) is widely recognized to be important. Contemporary interest arises from both controlling plasma-material interactions in the SOL, and in understanding the coupling of the SOL and edge plasmas to turbulent transport and confinement in the core. The importance of intermittent convective processes, in addition to diffusion, has been increasingly recognized in recent experimental¹⁻¹² and theoretical¹³⁻²⁴ papers (see also contained references for earlier works). Much of this literature has been devoted to the observation and description of convective transport as mediated by the propagation of coherent objects, referred to by various authors as meso-scale structures, fingers, streamers, filaments, intermittent plasma objects (IPOs), avaloids, or blobs.

The SOL width and possible main-chamber-plasma interactions²⁵ are governed by a competition between classical parallel flow and cross-field fluxes. Thus, it is important to understand the cross-field convective velocity of blobs. Early theories examined the sheath-connected limit.^{13,14,18,20} In this limit, the flow of parallel current is regulated by a sheath boundary condition at the termination point of the field lines, e.g. at the tokamak divertor plate. Other limits have also been studied within the context of two-dimensional (2D) models.²⁶⁻²⁸ In these approximate, but conceptually useful, reduced dimensionality models, different “closure” schemes for the parallel current are employed to account for effects such as field line bending²⁶ and magnetic X-points.^{23,26,28,29}

Previous work has shown that the parallel structure of linear modes is strongly influenced by the geometry of the magnetic field and the collisionality of the plasma.²⁸⁻³⁰ Analysis of three-dimensional (3D) fluid simulations has shown that the

same is true for blobs created by the turbulence associated with these linear modes.²³ As we shall show explicitly here, parallel structure can have a profound effect on the radial velocity of blobs: collisionality, acting synergistically with "fanned" magnetic geometry, leads to parallel disconnection of blobs from the sheaths, and results in a strong increase in the radial blob velocity into and across the SOL.

The inter-relationships among magnetic geometry, collisionality, and indirectly the spatial scale size of turbulent structures, are complex. So far a unified picture of the various regimes has not been available. In the present paper, we present an electrostatic two-region model which allows a transparent analysis of these effects. Our model, being an extension of previous 2D blob-turbulence models, is expected to be useful as an adjunct to full 3D simulations, and as a guide to understanding experiments and simulations.

The present paper is complementary to a previous study of instability and blob regimes which treated the limit of "disconnected" (from the sheath) structures using a Wentzel-Kramers-Brillouin (WKB) technique.²⁸ The work in Ref 28 considered both electrostatic and electromagnetic (line bending) effects, but cannot be readily extended to nonlinear simulations, or to situations in which partial or full connection to the sheaths occurs. These deficiencies motivated the present treatment.

In this, the first of two papers in a series, we present the basic two-region model, its analytic properties, and numerical simulations of the dynamics of prepared blobs. In a future publication, we will present the numerical simulation of fully developed turbulence in this model.

The plan of our paper is as follows. In Sec. II the two-region model is developed and its elementary properties are given. In particular, we consider the linear instabilities supported by the model and the conditions governing mode connection and disconnection from the sheaths. In Sec. III, we consider the model's invariant scalings and nonlinear properties. A regime diagram for blobs is given, and an analytical "blob dispersion

relation” for the speed of blob propagation is compared with numerical simulations. An inequality bounding the blob speed is obtained. Some details of the magnetic geometry, a limiting case for fully connected (low collisionality) solutions, and the relation of the model to other X-point models, are discussed in Appendices.

II. The two-region model

The two-region model is motivated by considering the geometry of a flux tube as it extends along the magnetic field and is influenced by the effects of fanning and shear. In the plane normal to \mathbf{B} , with local Cartesian variables $\mathbf{x} = (x, y)$, where x and y are the radial and binormal (approximately poloidal) directions, we consider the transformation that relates displacements perpendicular to the magnetic field at different positions along a field line

$$d\mathbf{x}_2 = \mathbf{M} \cdot d\mathbf{x}_1 \quad (1)$$

$$\mathbf{M} = \begin{pmatrix} g_1/g_2 & 0 \\ \xi & g_2 B_1 / (g_1 B_2) \end{pmatrix} \quad (2)$$

Here $g = RB_\theta$ describes the flux mapping (e.g. radial expansion of the flux surfaces near an X-point) and ξ is a metric coefficient describing the magnetic shear (see Appendix A). The determinant of \mathbf{M} is such that the total magnetic flux inside a flux tube is conserved, i.e. $B_1 dx_1 dy_1 = B_2 dx_2 dy_2$.

The basic equations of the 2D model in the plane normal to \mathbf{B} are the standard vorticity and continuity equations for two regions (each averaged along a portion of a field line), coupled by conservative charge flow (i.e. finite parallel conductivity) between the regions

$$(\partial_t + \mathbf{v}_1 \cdot \nabla_1) \nabla_1^2 \Phi_1 = \sigma_{12} (\Phi_1 - \Phi_2) / n_1 - \beta \partial_{y_1} \ln(n_1) \quad (3)$$

$$(\partial_t + \mathbf{v}_1 \cdot \nabla_1) n_1 = 0 \quad (4)$$

$$(\partial_t + \mathbf{v}_2 \cdot \nabla_2) \nabla_2^2 \Phi_2 = -\sigma_{12}(\Phi_1 - \Phi_2)/n_2 + \alpha \Phi_2 \quad (5)$$

$$(\partial_t + \mathbf{v}_2 \cdot \nabla_2) n_2 = 0 \quad (6)$$

where the convective $\mathbf{E} \times \mathbf{B}$ velocity is given by

$$\mathbf{v}_j = (\mathbf{e}_z \times \nabla \Phi)_j \quad (7)$$

and in the locally Cartesian space, $\mathbf{e}_z = \mathbf{b} = \mathbf{B}/B$. Here we employ the Bohm normalization (time scales normalized to $\Omega_i = eB/m_i c$, space scales to $\rho_s = c_s/\Omega_i$ where c_s is the sound speed based on the electron temperature T_e , and electrostatic potential Φ normalized to T_e/e). Similar equations have been employed as the starting point for semi-analytical work on disconnection (defined precisely below) and its relation to an edge plasma thermal catastrophe and associated density limit.³¹

In Eqs. (3) – (6), $\alpha = 2\rho_s/L_2$ where L_j is the length of field line in region j , $\beta = 2\rho_s/R$ where R is the major radius, and $\sigma_{12} = \rho_s^2 \Omega_i m_i / (L_{\parallel}^2 \eta_{\parallel} e^2)$ is a parallel conductivity coefficient that carries the dimension of density n . Note that curvature drive (β term) is included only in region 1, which we take as the outboard midplane region, and sheath charge loss (the α term) occurs only in region 2, the divertor (X-point) region. (More generally, a small curvature term could be included in region 2; however, the present simplification of neglecting curvature in region 2 adequately describes the tendency of modes to balloon at the outboard midplane, where the normal curvature maximizes, when other parameters do not force an interchange limit.) The sheath loss term $\alpha \Phi_2$ in Eq. (5) is a small Φ_2 approximation to the full nonlinear term¹⁴ $\alpha[1 - \exp(-\Phi_2)]$ that is usually well justified. For simplicity we consider the parallel lengths of both regions to be identical, i.e. $L_1 = L_2 \equiv L_{\parallel}$ although for perspicuity, the L_j notation will sometimes be employed. The gradients in the two regions are related by the metric tensor of Eq. (2), namely $\nabla_2 = \mathbf{M}^{-1, \text{tr}} \cdot \nabla_1$.

First consider the linear modes of the model. The effect of the transformation given by Eq. (1) when applied to X-point geometry is to enhance \mathbf{k}_\perp in both the x and y directions:³⁰ k_y is enhanced in region 2 as B_θ is reduced (the midplane to X-point flux surface mapping increases dx and decreases dy); k_x is enhanced by magnetic shear which accumulates along the field line. We consider the wavenumber in region 1, $\mathbf{k}_{\perp 1}$ to be given, determine $\mathbf{k}_{\perp 2}$ from the magnetic field line mapping, and seek a dispersion relation $\omega = \omega(\mathbf{k}_{\perp 1})$. Linearizing Eqs. (3) – (6) and performing straightforward algebra yields

$$\omega^2 + \gamma_{\text{mhd}}^2 + \frac{(i\omega\omega_{a1}^2/\omega_{\eta 1})(\omega + i\omega_{s2})}{i\omega_{a2}^2/\omega_{\eta 2} + \omega + i\omega_{s2}} = 0 \quad (8)$$

where the relative mode amplitudes in the two regions is

$$\frac{\delta\Phi_2}{\delta\Phi_1} = \frac{i\omega_{a2}^2/\omega_{\eta 2}}{\omega + i\omega_{a2}^2/\omega_{\eta 2} + i\omega_{s2}} \quad (9)$$

Here, we define characteristic frequencies (in Bohm units) as $\gamma_{\text{mhd}}^2 = -\beta(k_{y1}^2/k_{\perp 1}^2)\partial_x \ln n_1$, $\omega_{aj}^2/\omega_{\eta j} = \sigma_{12}/(n_j k_{\perp j}^2)$, and $\omega_{s2} = \alpha/k_{\perp 2}^2$. For reference, the characteristic frequencies in dimensional units are as follows: $\gamma_{\text{mhd}}^2 = -(2c_s^2/R)(k_{y1}^2/k_{\perp 1}^2)\partial_x \ln n_1$, $\omega_{aj} = v_a/L_j$ where v_a is the Alfvén velocity, $\omega_{\eta j} = \eta_{\parallel} k_{\perp j}^2 c^2/4\pi$ with parallel plasma resistivity η_{\parallel} , and $\omega_{sj} = 2c_s/(L_j k_{\perp j}^2 \rho_s^2)$. To obtain Eqs. (8) and (9) we take the equilibrium potentials as $\Phi_1 = \Phi_2 = 0$, or equivalently work in the $E \times B$ drifting frame.

To relate the wavenumbers in the two regions, define

$$\varepsilon_x = \frac{k_{\perp 1}}{k_{\perp 2}} \quad (10)$$

It will turn out that $\varepsilon_x \sim 1/f$ for $f \gg 1$ ($\varepsilon_x \sim f$ for $f \ll 1$), where the “fanning” f , introduced subsequently in Eqs. (26) and (B1), is a measure of the elliptical distortion of the flux surfaces.

The eigenfunctions are said to be “disconnected” from region 2 when $\delta\Phi_2 \ll \delta\Phi_1$ therefore from Eq. (9) the disconnection condition is

$$\frac{\omega_{a2}^2}{\omega_{\eta 2}} \ll \omega, \omega_{s2} \quad (11)$$

Disconnection is indicated at large resistivity and wavenumber.

The unstable spectrum starting at low $k_{\perp} \sim k_y$ for low collisionality, $\omega_s \omega_{\eta} < \omega_a^2$ or $\sigma_{12} > \alpha n$, is dominated by relatively slow growing ($\omega < \omega_{s2}$) sheath-connected (C_s) interchange modes³² that balance curvature drive in region 1 with parallel current flow to the sheaths in region 2,

$$\omega = \frac{i\gamma_{mhd}^2}{\omega_{s1}}, \quad k_{\perp} < k_{\perp a}, \quad (12)$$

At somewhat higher k_{\perp} , these revert to connected ideal-interchange (C_i) magnetohydrodynamic (MHD) modes that balance curvature drive in region 1 with (fanning enhanced) inertia (ion polarization drift) in region 2,

$$\omega = i\varepsilon_x \gamma_{mhd}, \quad k_{\perp a} < k_{\perp} < k_{\perp b}, \quad (13)$$

As k_{\perp} is increased still further, disconnection takes place at $\omega \omega_{\eta 2} = \omega_{a2}^2$ and one enters the resistive X-point (RX) -mode regime with growth rate

$$\omega = \frac{i\gamma_{mhd}^2 \omega_{\eta 1}}{\omega_{a1}^2}, \quad k_{\perp b} < k_{\perp} < k_{\perp c}, \quad (14)$$

The RX mode balances curvature drive in region 1 with parallel resistivity. Finally, at the highest k_{\perp} 's one obtains the largest growth rate, i.e. that of the resistive ballooning (RB) mode which balances curvature drive in region 1 with inertia in region 1

$$\omega = i\gamma_{\text{mhd}}, \quad k_{\perp c} < k_{\perp}, \quad (15)$$

The characteristic k_{\perp} 's at which these transitions happen are determined by equating the ω 's of the adjacent regimes:

$$\gamma_{\text{mhd}} = \varepsilon_x \omega_{s1} \Rightarrow k_{\perp a} \quad (C_s/C_i \text{ transition}) \quad (16)$$

$$\gamma_{\text{mhd}} \omega_{\eta 1} = \varepsilon_x \omega_a^2 \Rightarrow k_{\perp b} \quad (\text{disconnection} = C_i/\text{RX transition}) \quad (17)$$

$$\gamma_{\text{mhd}} \omega_{\eta 1} = \omega_a^2 \Rightarrow k_{\perp c} \quad (\text{RX/RB transition}) \quad (18)$$

These regime boundaries are consistent with applicable limits of the previous WKB treatment²⁸ (i.e. disconnected modes in the electrostatic limit) and in each regime, there is a corresponding circuit path for current flow along and across field lines (see e.g. Fig. 2 of Ref. 28); only the detailed expression (i.e. the powers of γ_{mhd} , ω_{η} and ω_a) for the RX regime growth rate differs in the two-region and WKB models. The WKB result for RX modes is $\omega = (-i)^{1/3} \gamma_{\text{mhd}}^{4/3} \omega_{\eta}^{1/3} / (4\omega_a^2)^{1/3}$ with all quantities evaluated in the midplane region. Unlike the WKB treatment, the two-region model, Eqs. (3) – (6), is nonlinear in the field variables, and it allows a unified description of both the sheath-connected (C_s , C_i) and disconnected regimes (RX, RB).

In the two limiting cases of large and small collisionality, the two-region model reduces to a one-region description. The fully disconnected RB regime is clearly described by region 1 alone. The fully connected limit can be treated by an appropriate field-line-average over both regions and is considered in Appendix B.

This completes a description of the model and some of its elementary properties. A discussion of the relation of the present model to other X-point models, in particular that of Ref. 29, is given in Appendix C. In the next section we consider the model's invariant scalings and nonlinear properties.

III. Blob regimes and velocity scaling

It is useful to apply the invariant scaling analysis of Connor and Taylor³³ to Eqs. (3) – (6). The first step in this method is to postulate the scale change $\Phi \rightarrow \lambda \Phi$. Then one seeks transformations for all other dependent and independent variables that leave the original equations invariant (i.e. independent of λ). Making an ansatz of the form $t \rightarrow \lambda^a t$, $\mathbf{x} \rightarrow \lambda^b \mathbf{x}$, similarly for σ_{12} , β , $q \equiv \beta/\alpha = L_{\parallel}/R$, and n with unknown exponents a , b , ... it can be shown that an invariant scaling is given by

$$\begin{aligned} \Phi &\rightarrow \lambda \Phi, n \rightarrow \lambda^{-v} n, \mathbf{x} \rightarrow \mathbf{x}/\lambda^{1-\mu}, t \rightarrow t/\lambda^{3-2\mu}, \\ \sigma_{12} &\rightarrow \lambda^{5-4\mu-v} \sigma_{12}, \beta \rightarrow \lambda^{5-3\mu} \beta, q \rightarrow \lambda^{\mu} q \end{aligned} \quad (19)$$

where μ and v are free parameters.

Any physical result arising from the solution of the original equations, e.g. a function $F(\sigma_{12}, \beta, q; n, \Phi; \mathbf{x}, t)$ must be independent of λ for all μ and v (i.e. invariant) since they are arbitrary. This forces the arguments of F to appear only in certain combinations. Two such invariant combinations are

$$\Lambda = \frac{n_{\text{ref}} \alpha}{\sigma_{12}} = \frac{v_{ei} L_{\parallel}}{\Omega_e \rho_s} = \frac{\omega_{\eta 1} \omega_{s1}}{\omega_{a1}^2} \quad (20)$$

and

$$\Theta = \hat{a}^{5/2} = \left(\frac{a_b}{a_*} \right)^{5/2} = \frac{\omega_{s1}}{\gamma_{\text{mhd}}} \quad (21)$$

where n_{ref} is a reference density, $\hat{a} \equiv a_b / a_*$ and $a_* = (q/\alpha)^{1/5}$. Here a_b is a spatial scale size which will soon be identified with a nominal blob radius. Furthermore, introducing a dimensionless frequency, which is also invariant under Eq. (19),

$$\hat{\omega} = \frac{\omega}{\gamma_{\text{mhd}}} \quad (22)$$

we obtain the dispersion relation, Eq. (8), in dimensionless form as

$$1 + \hat{\omega}^2 + \frac{i\hat{\omega}\Theta(\hat{\omega} + i\varepsilon_x^2\Theta)}{i\varepsilon_x^2\Theta + \Lambda(\hat{\omega} + i\varepsilon_x^2\Theta)} = 0 \quad (23)$$

Moreover, the invariant scaling applies to the full nonlinear equations of the model, not just to the linear modes. Thus, the nonlinear evolution (and in particular the velocity) of a blob with parameters $(n, a_b, \sigma_{12}, \beta, \alpha)$ is determined solely by Θ and Λ for a fixed model geometry (here ε_x or f); i.e., the five original blob parameters are reduced to two by means of the three degrees of freedom in the scaling transformation $(\mu, \nu$ and $\lambda)$.

Next, we postulate a *blob correspondence rule* that relates the linear instability growth rate $\text{Im}(\omega)$ to the blob convection velocity

$$\text{Im}(\omega) \rightarrow v_x / a_b \quad (24)$$

together with $(L_n, 1/k) \rightarrow a_b$, and $1/k_{\parallel} \rightarrow L_{\parallel}$. This rule, and the nonlinear blob dispersion relation discussed subsequently, makes explicit the correspondence between linear stability and turbulent transport noted in Ref. 34 for sheath-driven interchange modes and generalizes it to more collisional instability regimes. It is based on the observation that for coherent nonlinear propagation of density, the ∂_t and $\mathbf{v} \cdot \nabla$ terms in the continuity equation must approximately balance.

A useful characteristic velocity for blobs is $v_* = (a_*\beta)^{1/2}$ which is the velocity in the RB regime for the case $a_b = a_*$. [See Eq. (28) for the dimensional definition.] Defining the invariant velocity $\hat{v} = v_x / v_*$ yields the blob correspondence rule in invariant scaling as

$$\hat{v} = \text{Im}(\hat{\omega}) \hat{a}^{1/2} = \text{Im}(\hat{\omega}) \Theta^{1/5} \quad (25)$$

Thus, a ‘‘blob dispersion relation’’ $\hat{v} = \hat{v}[\Lambda, \Theta(\hat{a}), \varepsilon_x]$ is obtained immediately from Eqs. (23) and (25). We note, in particular, the low collisionality, small \hat{a} limit, $\hat{v} = 1/\hat{a}^2$ which is just the familiar sheath-connected scaling^{13,14} and the high collisionality, large

\hat{a} limit, $\hat{v} = \hat{a}^{1/2}$ which is the RB scaling, noted in Refs. 16, 23, 28, and also recently in Ref. 24 (where it is referred to as inertial scaling).

Since the dynamics is completely specified by Θ, Λ for given ε_x , it is useful to characterize the system by regimes in the (Θ, Λ) plane. The resulting blob regime diagram is shown in Fig. 1. The same regime boundaries characterize the linear modes and nonlinear convective velocities. Four distinct regimes, akin to Eqs. (12) – (15) are apparent. In the sheath-interchange (C_s) and ideal-interchange (C_i) regimes the midplane and X-point regions are electrically connected; in the resistive X-point (RX) and resistive ballooning (RB) regimes they are disconnected. Scalings for $\hat{\omega}$ and \hat{v} , given in the figure, show continuity at all boundaries. These scalings are derived from the appropriate asymptotic limits of the (blob) dispersion relation, Eqs. (23) and (25).

We have employed numerical simulations to test these scalings and more generally, the blob correspondence principle, Eq. (24). In these simulations, a blob of a given size was initialized far from the simulation boundaries, and its velocity was measured after transients but before blob break-up (e.g. due to secondary instabilities^{16,35}). We neglected magnetic shear between the two regions in this study and assumed $B_1 = B_2$ (large aspect ratio tokamak) so that the geometry of the two regions are related by the simple area-preserving transformation

$$\frac{\partial}{\partial x_2} = f \frac{\partial}{\partial x_1}, \quad \frac{\partial}{\partial y_2} = \frac{1}{f} \frac{\partial}{\partial y_1} \quad (26)$$

which defines the “fanning factor” f . This describes an X-point-induced elliptical distortion of a circular flux tube.³⁶ [Also see Eqs. (1), (2) and Appendix A.]

The results of these simulation measurements for the case $f = 4$, $\varepsilon_x = 0.25$ are compared directly to the solution of the full blob dispersion relation in Fig. 2. The agreement confirms the blob correspondence principle to within factors of order unity or better. The results of Fig. 2 show that the blob velocity increases with collisionality for

all blob sizes. The scaling of velocity with size depends on the collisionality regime, as noted following Eq. (25). In particular, the simulations confirm that \hat{v} decreases with \hat{a} for small Λ (sheath-interchange scaling), but increases with \hat{a} for large Λ (RB scaling).

Figure 3 shows the simulation results for the blob density in the (x, y) plane in region 1 (midplane region) for four different values of collisionality, corresponding to the $\Theta = 316$ case shown in Fig. 2. Blobs were initialized at $\hat{t} = 0$ at the dashed line to avoid interaction with the simulation boundary. The full simulation domain is shown in each panel, at the invariant time $\hat{t} = t \gamma_{\text{mhd}} = t(\beta/a)^{1/2} = 12.6$. The differences in nonlinear evolution and speed are evident. Faster blobs tend to be more vulnerable to secondary instability. The most extreme fully disconnected case ($\Lambda = 1000$) is unstable to Kelvin-Helmholtz modes.¹⁶ A very small floor density (1% of the blob peak density) was employed in these simulations.

An important byproduct of the analysis of this section is that it allows simple analytical bounds on the blob convective velocity as a function of their scale size a_b (nominal blob radius) within electrostatic theory. From the small and large Λ limits, which respectively give the lower (sheath-connected) and upper (RB) bounds, we obtain.

$$\frac{1}{\hat{a}^2} < \hat{v} < \hat{a}^{1/2} \quad (27)$$

where, to repeat, $\hat{v} = v_x / v_*$, $\hat{a} = a_b / a_*$, and in dimensional units

$$v_* = c_s \left(\frac{a_*}{R} \right)^{1/2} \quad (28)$$

$$a_* = \frac{\rho_s^{4/5} L_{\parallel}^{2/5}}{R^{1/5}} \quad (29)$$

An application of the regime diagram to the National Spherical Torus Experiment³⁷ (NSTX) and Alcator C-Mod³⁸ experiments, and a detailed experimental test of Eq. (27) on NSTX is described elsewhere.³⁹

IV. Conclusions

In this paper, we have proposed an electrostatic two-region model, Eqs. (3) – (6), for reduced simulation of 3D effects, and explored its linear and nonlinear properties. The model extends previous 2D models for edge and SOL turbulent transport by taking into account the parallel structure of the turbulence in response to collisionality, magnetic field fanning and shear, which is particularly important in divertor X-point geometry. Previous work could describe some effects of a magnetic X-point on linear instability and blob propagation by using a parallel (along B) boundary condition as a closure for the parallel current. However, the present model also allows a description of the phenomenon of disconnection, i.e. the breaking of the electrical connection along B due to parallel resistivity.

We employed an invariant scaling analysis to show that there are two irreducible parameters of the model chosen to be the collisionality parameter Λ and a spatial scale parameter \hat{a} or $\Theta = \hat{a}^{5/2}$ defined by Eqs. (20) and (21). A blob correspondence rule relating the linear instability growth rates to the nonlinear blob convective velocity was proposed in Eq. (24) and used to construct a “blob dispersion relation,” Eqs. (23) and (25), for the convective velocity. One key result of our paper is the regime diagram of Fig. 1, showing the four regimes of electrostatic blob convection in the Θ, Λ parameter space. Disconnected regimes (RB and RX) occur for large Λ and/or small Θ and are facilitated by magnetic geometry (small ε_x) arising from magnetic shear and flux tube distortion.

The validity of the correspondence rule and blob dispersion relation analysis was tested by numerical simulations of blob convection. These simulations showed good qualitative agreement with the analytic model and scalings, and verified the importance of disconnection in increasing the blob propagation speed (see Fig. 2). We found that the speed increases with Λ but scales with \hat{a} differently in each collisionality regime. In the extreme case of low collisionality we recover the sheath-interchange scaling,

$\hat{v} = 1/\hat{a}^2$ and in the opposite extreme case of high collisionality we recover the RB (inertial) scaling result $\hat{v} = \hat{a}^{1/2}$. This observation allows simple analytical bounds on the blob velocity in electrostatic theory, Eqs. (27) – (29), to be obtained in terms of a characteristic velocity v_* . For the ubiquitous situation of curvature driven modes, these analytical velocity bounds may be useful as the basis for experimental tests of the concepts elucidated by the two-region model, namely, the collisionality, scale size and geometry dependence of blob convection, and the underlying scalings and regimes.

Generalizations of the present model to include equations for the electromagnetic response, temperature evolution and parallel flows may be useful. Electromagnetic effects on blobs,^{26–28} of interest for edge-localized-mode (ELM) studies, could be implemented in a two-region model to describe parallel structure and the connected - disconnected transition. (The boundaries for which electromagnetic effects become important are given in Ref. 28.) Other instability drive terms may also be of interest for blob studies using the two-region model, e.g. drift-wave effects,¹⁸ E×B parallel shear modes,⁴⁰ and the temperature-gradient driven “conducting wall” mode.⁴¹ The importance of these effects on blob propagation in a given situation can usually be estimated by comparing the relevant instability growth rate with γ_{mhd} . Reduced models of nonlinear SOL transport, such as the two-region model proposed here and its generalizations, merit further exploration as a guide to understanding the complicated behavior of edge turbulence experiments and simulations.

Acknowledgments

This work was supported by the U.S. Department of Energy (DOE) under grant DE-FG02-97ER54392; however, such support does not constitute an endorsement by the DOE of the views expressed herein.

Appendix A: Magnetic geometry

In this appendix, we consider the mapping of a flux tube along \mathbf{B} . A flux tube is defined by first specifying a central starting vector \mathbf{r} in three-dimensional space corresponding to flux variables (ψ, θ, ζ) giving poloidal flux, poloidal angle and toroidal angle respectively. Here $\mathbf{e}_\psi = \nabla\psi/|\nabla\psi|$ and $\mathbf{e}_\theta = \nabla\theta/|\nabla\theta|$ are not necessarily orthogonal. The geometry of the flux tube can be parameterized by dr_ψ and dr_χ where

$$d\mathbf{r}_\perp = dr_\psi \mathbf{e}_\psi + dr_\chi \mathbf{e}_\chi \quad (\text{A1})$$

and $(\mathbf{e}_\psi, \mathbf{e}_\chi = \mathbf{b} \times \mathbf{e}_\psi, \mathbf{b})$ form a locally orthogonal coordinate system. Thus $d\mathbf{r}_\perp$ is the variation in the flux tube orthogonal to \mathbf{B} , where

$$\mathbf{B} = v \nabla\psi \times \nabla\theta + \nabla\zeta \times \nabla\psi \equiv \mathbf{B}_\zeta + \mathbf{B}_\theta \quad (\text{A2})$$

The goal here is to define the transformation which maps (dr_ψ, dr_χ) along \mathbf{B} . In this Appendix, the starting position of the flux tube is described by unadorned symbols and the mapped coordinates along \mathbf{B} are denoted by primes. For application to the midplane and X-point regions in the main text, these correspond to subscripts 1 and 2 respectively.

We first introduce the compact notations, $d\mathbf{F} = (d\psi, d\theta, d\zeta)$ and $d\mathbf{r} = (dr_\psi, dr_\chi, dr_\parallel)$. We seek the coordinate transformation $d\mathbf{F} = \mathbf{T} \cdot d\mathbf{r}$. This is obtained by using $d\psi = d\mathbf{r} \cdot \nabla\psi$, $d\theta = d\mathbf{r} \cdot \nabla\theta$, $d\zeta = d\mathbf{r} \cdot \nabla\zeta$ together with the identity matrix representation $\mathbf{I} = \mathbf{e}_\psi \mathbf{e}_\psi + \mathbf{e}_\chi \mathbf{e}_\chi + \mathbf{b} \mathbf{b}$. Thus, $d\theta = \nabla\theta \cdot \mathbf{I} \cdot d\mathbf{r} = \nabla\theta \cdot \mathbf{e}_\psi dr_\psi + \nabla\theta \cdot \mathbf{e}_\chi dr_\chi + \nabla\theta \cdot \mathbf{b} dr_\parallel$ and similarly for $d\psi$ and $d\zeta$. The matrix \mathbf{T} that results is

$$\mathbf{T} = \begin{pmatrix} \nabla\psi \cdot \mathbf{e}_\psi & 0 & 0 \\ \nabla\theta \cdot \mathbf{e}_\psi & \nabla\theta \cdot \mathbf{e}_\chi & \nabla\theta \cdot \mathbf{b} \\ 0 & \nabla\zeta \cdot \mathbf{e}_\chi & \nabla\zeta \cdot \mathbf{b} \end{pmatrix} \quad (\text{A3})$$

We can determine the matrix elements explicitly. From the definition of ψ as poloidal flux, $\nabla\psi \cdot \mathbf{e}_\psi = |\nabla\psi| = RB_\theta$. Furthermore $\nabla\theta \cdot \mathbf{e}_\psi = \nabla\theta \cdot \nabla\psi / (RB_\theta) = -\gamma RB_\theta / v$ directly from the definition of γ in Eq. (A11). For $\nabla\theta \cdot \mathbf{e}_\chi$ we first employ the definition of

\mathbf{e}_χ to obtain $\nabla\theta\cdot\mathbf{e}_\chi = b_\zeta\nabla\theta\cdot\mathbf{e}_\zeta\times\mathbf{e}_\psi$ where $b_\zeta = B_\zeta/B$. Then dotting Eq. (A2) by \mathbf{e}_ζ it follows that $\nabla\theta\cdot\mathbf{e}_\zeta\times\mathbf{e}_\psi = B_\zeta/(vRB_\theta)$ so that the desired matrix element is $\nabla\theta\cdot\mathbf{e}_\chi = B_\zeta^2/(vBRB_\theta)$. Next, $\nabla\theta\cdot\mathbf{b}$ is obtained by dotting Eq. (A2) by $\nabla\theta$ and again performing the same elimination of $\nabla\theta\cdot\mathbf{e}_\zeta\times\mathbf{e}_\psi$ to yield $\nabla\theta\cdot\mathbf{b} = B_\zeta/(vBR)$. Turning to $\nabla\zeta\cdot\mathbf{e}_\chi = \mathbf{e}_\zeta\cdot\mathbf{e}_\chi/R$ we employ the definition of \mathbf{e}_χ to obtain immediately $\nabla\zeta\cdot\mathbf{e}_\chi = -B_\theta/(RB)$. Finally, $\nabla\zeta\cdot\mathbf{b} = B_\zeta/(RB)$. Summarizing

$$\mathbf{T} = \begin{pmatrix} RB_\theta & 0 & 0 \\ -\gamma RB_\theta/v & B_\zeta^2/(vBRB_\theta) & b_\zeta/(vR) \\ 0 & -b_\theta/R & b_\zeta/R \end{pmatrix} \quad (\text{A4})$$

The next step in describing the flux tube geometry is to relate the restricted class of displacements (dr_ψ, dr_χ) in Eq. (A1) to $(d\psi, d\theta, d\zeta)$. For this, we set $dr_{\parallel} = \mathbf{dr}\cdot\mathbf{b} = 0$ in the general transformation to obtain $d\mathbf{F} = \mathbf{T}\cdot d\mathbf{r}_\perp$, or explicitly

$$d\psi = RB_\theta dr_\psi \quad (\text{A5})$$

$$d\theta = \frac{-\gamma RB_\theta}{v} dr_\psi + \frac{B_\zeta^2}{vBRB_\theta} dr_\chi \quad (\text{A6})$$

$$d\zeta = \frac{-B_\theta}{RB} dr_\chi \quad (\text{A7})$$

The constraint that $dr_{\parallel} = 0$, is $\mathbf{b}\cdot\mathbf{T}^{-1}\cdot d\mathbf{F} = 0$. We find

$$\mathbf{T}^{-1} = \begin{pmatrix} 1/RB_\theta & 0 & 0 \\ \gamma Rb_\theta & Rvb_\theta & -Rb_\theta \\ \gamma RB_\theta^2/(BB_\zeta) & RvB_\theta^2/B_\zeta B & Rb_\zeta \end{pmatrix} \quad (\text{A8})$$

therefore the constraint can be expressed as

$$\gamma d\psi + vd\theta + (B_\zeta/B_\theta)^2 d\zeta = 0 \quad (\text{A9})$$

where \mathbf{v} is the local rotational transform

$$\zeta' = \zeta + \int_{\theta}^{\theta'} d\theta \mathbf{v} \quad (\text{A10})$$

and

$$\gamma = -\frac{\mathbf{v}}{R^2 B_{\theta}^2} \nabla \theta \cdot \nabla \psi \quad (\text{A11})$$

Equations (A5) – (A7) yield the first mapping $(dr_{\psi}, dr_{\chi}) \rightarrow (d\psi, d\theta, d\zeta)$. It may be verified directly that this mapping satisfies the constraint of orthogonality to \mathbf{B} , Eq. (A9).

Next, Eq. (A10) and $\psi' = \psi$ are employed to map the flux tube's central field line along \mathbf{B} from a point $\mathbf{F} = (\psi, \theta, \zeta)$ to $\mathbf{F}' = (\psi', \theta', \zeta')$. The flux tube geometry $(d\psi, d\theta, d\zeta)$ at \mathbf{F} is similarly mapped to $(d\psi', d\theta', d\zeta')$ at \mathbf{F}' by the relations $d\psi' = d\psi$, and

$$d\zeta' = d\zeta + d\theta' \mathbf{v}' - d\theta \mathbf{v} + d\psi(\gamma' - \beta' + \beta - \gamma) \quad (\text{A12})$$

[obtained by taking differentials of Eq. (A10)] where β (introduced for later convenience) quantifies the field-line-integrated magnetic shear and is defined by

$$\frac{\partial \beta}{\partial \theta} \equiv \frac{\partial \gamma}{\partial \theta} - \frac{\partial \mathbf{v}}{\partial \psi} \quad (\text{A13})$$

Next $d\zeta$ and $d\zeta'$ are eliminated from Eq. (A12) by employing the two orthogonality constraints, Eq. (A9), and its equivalent in primed variables. The result is an expression which describes the mapping along \mathbf{B} as

$$\tau' d\theta' = \tau d\theta + (\sigma - \sigma') d\psi \quad (\text{A14})$$

where $\sigma = \gamma B^2 / B_{\zeta}^2 - \beta$ and $\tau = \mathbf{v} B^2 / B_{\zeta}^2$. Note that throughout the derivation, the assumption of toroidally axisymmetric geometry renders all scalars (B_{θ} , B_{ζ} , \mathbf{v} , γ , β , σ , τ) independent of ζ .

The final step is to relate $(d\psi', d\theta', d\zeta')$ to (dr_{ψ}', dr_{χ}') . This is done using the inverse procedure to that described by Eqs. (A4) – (A7), $d\mathbf{r}' = \mathbf{T}'^{-1} \cdot d\mathbf{F}'$, together with the orthogonality constraint, and results in

$$dr_{\psi}' = \frac{d\psi'}{R'B_{\theta}'} \quad (\text{A15})$$

$$dr_{\chi}' = \frac{R'B_{\theta}'B'}{B_{\zeta}'^2}(\gamma'd\psi' + \nu'd\theta') \quad (\text{A16})$$

Collecting together the three parts of the transformation, $(dr_{\psi}, dr_{\chi}) \rightarrow (d\psi, d\theta, d\zeta) \rightarrow (d\psi', d\theta', d\zeta') \rightarrow (dr_{\psi}', dr_{\chi}')$, yields, after some algebra

$$\begin{pmatrix} dr_{\psi}' \\ dr_{\chi}' \end{pmatrix} = \begin{pmatrix} g/g' & 0 \\ \xi & g'B/(gB') \end{pmatrix} \begin{pmatrix} dr_{\psi} \\ dr_{\chi} \end{pmatrix} \quad (\text{A17})$$

where $g = RB_{\theta}$ and $\xi = gg'(\beta' - \beta)/B'$. This establishes Eqs. (1) and (2) of the main text. The ratio $g'/g \equiv f$ is referred to as the flux-tube “fanning” in this paper and ξ is a magnetic shear factor.

The present formalism for the geometry of an infinitesimal flux tube is closely related to the eikonal formalism for the propagation of a wave-vector \mathbf{k} along a field line under the constraint that $k_{\parallel} = 0$ (See e.g. Ref. 30). Defining $d\mathbf{x} = (dr_{\psi}, dr_{\chi})$, $d\mathbf{x}' = (dr_{\psi}', dr_{\chi}')$ and

$$d\mathbf{x}' = \mathbf{M} \cdot d\mathbf{x} \quad (\text{A18})$$

with \mathbf{M} given by Eq. (A17), we identify

$$i\mathbf{k}_{\perp} = \frac{\partial}{\partial \mathbf{x}} \quad (\text{A19})$$

Then it follows that $\mathbf{k}_{\perp} = \mathbf{M}^{\text{tr}} \cdot \mathbf{k}'_{\perp}$ where tr is the transpose operation. After some algebra to extract the $(\mathbf{e}_{\psi}, \mathbf{e}_{\theta}, \mathbf{e}_{\zeta})$ components of $\mathbf{k} = \mathbf{k}_{\perp}$, and further taking $k_{\zeta} = n_{\zeta}/R$

where n_ζ is the toroidal mode number, it can be shown that $k'_\zeta = n_\zeta/R'$, $k'_\psi = n_\zeta R' B'_\theta (\beta' - \beta)$ and $k'_\chi = -n_\zeta B' / R' B'_\theta$ which is the eikonal result.

Appendix B: Fully connected solutions

In the limiting case of sufficiently weak collisionality, $\Lambda \rightarrow 0$, the solutions of the two-region model become fully connected, i.e. interchange-like with $\Phi_1 = \Phi_2$. This limit is explored in the following, where we show that the problem is isomorphic to an equivalent one-region-model problem. Our analysis takes into account fanning f and shear ξ in the magnetic flux mapping between the regions.

The starting equations are Eqs. (3) – (6) of the main text, with the two regions related by $d\mathbf{x}_2 = \mathbf{M} \cdot d\mathbf{x}_1$. Here \mathbf{M} is taken from Eq. (2) with $B_1 = B_2$ (for a large aspect ratio tokamak), and we define $f = g_2/g_1$, so that

$$\mathbf{M} = \begin{pmatrix} 1/f & 0 \\ \xi & f \end{pmatrix} \quad (\text{B1})$$

where f and ξ are constants. It follows that

$$\nabla_2 = \mathbf{M}^{-1, \text{tr}} \cdot \nabla_1 \quad (\text{B2})$$

$$\mathbf{M}^{-1, \text{tr}} = \begin{pmatrix} f & -\xi \\ 0 & 1/f \end{pmatrix} \quad (\text{B3})$$

where -1 and tr are the matrix inversion and transpose operations respectively.

In the limit $\sigma_{12} \rightarrow \infty$, $\Phi_1 = \Phi_2 \equiv \Phi$ is guaranteed from the vorticity equations. Writing out the components of Eq. (B2) and eliminating $\partial/\partial x_2$ and $\partial/\partial y_2$ in terms of $\partial/\partial x_1$ and $\partial/\partial y_1$ in $\mathbf{v}_2 \cdot \nabla_2$ it follows that $\mathbf{v}_2 \cdot \nabla_2 = \mathbf{v}_1 \cdot \nabla_1$. Then, the two continuity equations, Eqs. (4) and (6), become identical, allowing us to take $n_1 = n_2 \equiv n$. Returning to the vorticity equations, and performing an interchange average by taking the sum of the two equations yields

$$\left(\frac{\partial}{\partial t} + \mathbf{v}_1 \cdot \nabla_1\right) \left(\nabla_1^2 + \nabla_2^2\right) \Phi = \alpha \Phi - \frac{\beta}{n} \frac{\partial n}{\partial y_1} \quad (\text{B4})$$

We again eliminate $\partial/\partial x_2$ and $\partial/\partial y_2$ in terms of $\partial/\partial x_1$ and $\partial/\partial y_1$ in ∇_2^2 to obtain

$$\nabla_1^2 + \nabla_2^2 = \partial_x^2 + (f \partial_x - \xi \partial_y)^2 + (1 + 1/f^2) \partial_y^2 \quad (\text{B5})$$

where, on the right-hand-side of Eq. (B5) and future equations, we suppress the subscript 1 on x and y , henceforth referring all quantities to region 1.

Next, we seek a change of variables that transforms Eq. (B4) into the standard form of the one-region model. Introducing \mathbf{x}' (no relation to the prime notation used in Appendix A) by

$$\begin{pmatrix} \partial_{x'} \\ \partial_{y'} \end{pmatrix} = \begin{pmatrix} a & b \\ 0 & c \end{pmatrix} \cdot \begin{pmatrix} \partial_x \\ \partial_y \end{pmatrix} \quad (\text{B6})$$

the desired simplification can be achieved by the choices

$$a = \sqrt{1 + f^2} \quad (\text{B7})$$

$$b = \frac{-f \xi}{\sqrt{1 + f^2}} \quad (\text{B8})$$

$$c = \sqrt{1 + 1/f^2 + \xi^2/(1 + f^2)} \quad (\text{B9})$$

Under Eq. (B6), or equivalently

$$\begin{pmatrix} \partial_x \\ \partial_y \end{pmatrix} = \begin{pmatrix} 1/a & -b/(ac) \\ 0 & 1/c \end{pmatrix} \cdot \begin{pmatrix} \partial_{x'} \\ \partial_{y'} \end{pmatrix} \quad (\text{B10})$$

it can be shown that $\nabla_1^2 + \nabla_2^2 = \nabla'^2$. Also noting that $\mathbf{v} \cdot \nabla = \mathbf{v}' \cdot \nabla'/(ac)$, the field-line-averaged vorticity equation becomes

$$\left(\frac{\partial}{\partial t} + \frac{1}{ac} \mathbf{v}' \cdot \nabla'\right) \nabla'^2 \Phi = \alpha \Phi - \frac{\beta}{cn} \frac{\partial n}{\partial y'} \quad (\text{B11})$$

Finally, introducing a new time variable

$$t' = t/(ac) \quad (\text{B12})$$

and defining

$$\alpha' = ac \alpha \quad (\text{B13})$$

$$\beta' = a \beta \quad (\text{B14})$$

we obtain the following vorticity and continuity equations

$$\left(\frac{\partial}{\partial t'} + \mathbf{v}' \cdot \nabla' \right) \nabla'^2 \Phi = \alpha' \Phi - \frac{\beta'}{n} \frac{\partial n}{\partial y'} \quad (\text{B15})$$

$$\left(\frac{\partial}{\partial t'} + \mathbf{v}' \cdot \nabla' \right) n = 0 \quad (\text{B16})$$

Equations (B15) and (B16) are just the standard one-region-model equations. Thus we have shown that in the limit of small collisionality, where the mode and blob structures are interchange-like, the two-region model is isomorphic to an equivalent one-region problem. This result is useful both for code benchmarking and for insight into the effect of magnetic geometry (f and ξ) on small Λ cases.

As a sample application of the isomorphism, we consider an analytic blob solution¹⁴ to Eqs. (B15) and (B16) in the limit where the inertial term on the left-hand-side of Eq. (B15) is negligible (C_s regime). A solution is

$$n = n_0 \exp\left(-\rho^2 / 2a_b'^2\right) \quad (\text{B17})$$

where

$$\rho^2 = (x' - v'_x t')^2 + y'^2, \quad (\text{B18})$$

a_b' is the blob radius, and its velocity is $v'_x = \beta' / (\alpha' a_b'^2)$. Transforming back to unprimed variables (region 1) provides an exact solution of the original problem in the C_s regime. Employing $x' = x/a$, $y' = y/c - bx/(ac)$, we immediately find

$$\rho^2 = \frac{1}{a^2} \left(x - \frac{\beta}{\alpha c^2 a'_b} t \right)^2 + \frac{1}{c^2} \left(y - \frac{b}{a} x \right)^2 \quad (\text{B19})$$

Thus in region 1 the nominal scale size in y (at fixed x) is $a_y = ca'_b$, the velocity is $v_x = \beta/(\alpha a_y^2)$, and the scale size in x (at fixed y) is $a_x = aca'_b/(b^2 + c^2)^{1/2}$. When $\xi \neq 0$ the blob is a tilted ellipse in the x - y plane and has finite $v_y = (b/a)v_x$. A slight generalization of this solution is obtained by noting that any x' dependence of the blob in Eq. (B17) is still a solution. In particular, one can introduce $a'_{bx} \neq a'_{by}$ to obtain blobs that have $a_x = a_y$ in region 1 for any choices of f and ξ . This analytical solution is instructive for physical insight, but like the one-region solution from which it is derived, it must be remembered that it is subject to secondary instabilities,^{16,35} and the effect of background plasma (a small amount of which moves the charges from $y = \pm\infty$ to finite y).

A similar heuristic analysis is possible in the C_i regime, although an exact solution of the isomorphic one-region problem is not possible. In this case the blob velocity in the primed frame is estimated as $v'_x = (\beta'a'_b)^{1/2}$. The rest of the analysis goes through as before resulting in the same shearing rate and scale size estimates for a_x and a_y , but now the velocity is given by $v_x = (\beta a_x)^{1/2}/c$. Specializing to the case $f \sim 1/\xi \sim O(\epsilon_x)$ we find $c \sim 1/\epsilon_x$ and therefore $v_x \sim \epsilon_x v_{RB}$ consistent with the estimate given in the regime diagram of Fig. 1.

Appendix C: Relation to other X-point models

The present two-region model may be compared with previous work^{23,26,28,29} in which X-point effects have been treated by different methods. In all these treatments the important role of X-point fanning is to increase the k_\perp of the modes in the X-point region.³⁶ Intuitively, we expect that cross-field current flow will be facilitated by thin magnetic flux “fans”. Two different cross-field current mechanisms in the X-point region, both important because of enhanced k_\perp , have been considered. In the present

model, the estimates of Ref. 23, and in the WKB treatment of Ref. 28, the enhanced perpendicular current is the ion polarization current $J_{\perp\text{pol}} = -\sigma_{\perp\text{pol}}\nabla_{\perp}\Phi$ where, for the linear polarization drift term [$J_{\perp\text{pol}} \propto (d/dt)\nabla_{\perp}\Phi \rightarrow \partial_t\nabla_{\perp}\Phi$], we have $\sigma_{\perp\text{pol}} = -i(c^2\omega/4\pi v_a^2)$. This results in $\nabla \cdot J_{\perp\text{pol}} \propto k_{\perp}^2$. As k_{\perp} increases to the point where $k_{\perp}\rho_i \gg 1$, a different mechanism occurs. The ions become unresponsive to the electric field because of gyro-orbit averaging, but perpendicular current can be carried collisionally by electrons resulting in $\sigma_{\perp\text{ve}} = \omega_{pe}^2 v_e / 4\pi\Omega_e^2$ as discussed in Ref. 29.

Turning from WKB theory to the two-region model, it is straightforward to extend the dispersion relation of Eq. (8) to include both mechanisms by including the appropriate perpendicular currents on the left-hand-side of Eq. (5). In Eq. (8), this results in the replacement $\omega + i\omega_s \rightarrow \omega + i\omega_s + i(\sigma_{\perp\text{ve}}/n_2)(L_v/L_{\text{pol}})(k_{\perp v}/k_{\perp\text{pol}})^2$ (without modifying the other terms involving ω) where L_v and L_{pol} are the parallel lengths over which each mechanism is operative and $k_{\perp v}/k_{\perp\text{pol}}$ is the ratio of wavenumbers in each region respectively. Here, the dimensionless collisional conductivity is $\sigma_{\perp\text{ve}} = v_e/\Omega_e$. One can then determine the resulting modifications to the regime diagram. Regimes that are disconnected by the polarization drift mechanism remain so. When the $\sigma_{\perp\text{pol}}$ mechanism is too weak to trigger disconnection, the $\sigma_{\perp\text{ve}}$ mechanism can enter. (Note that the modes will experience the $k_{\perp}\rho_i < 1$, $\sigma_{\perp\text{pol}}$ mechanism first as they penetrate the X-point region, then as $k_{\perp}\rho_i > 1$ occurs further downstream, the $\sigma_{\perp\text{ve}}$ mechanism takes over.) For comparison purposes, it can be shown that the ratio $\sigma_{\perp\text{ve}}/\sigma_{\perp\text{pol}} \sim \Lambda c_s/(\omega L_{\parallel})$. In the regimes that remain connected by the polarization current mechanism we have $\Lambda < 1$ and typically $\omega \gg c_s/L_{\parallel}$. Thus, the condition for collisionally-assisted disconnection is $(L_v/L_{\text{pol}})(k_{\perp v}/k_{\perp\text{pol}})^2 \gg \omega L_{\parallel}/(\Lambda c_s) \gg 1$ where the first ratio in these inequalities is determined by the magnetic geometry of the X-point configuration, and the midplane k_{\perp} of the mode.

As a matter of practical consideration, the various X-point boundary conditions or closure schemes have interesting features and shortcomings. For WKB applications, in

which the modes are fully disconnected from end sheaths, the boundary condition on the parallel current at the entrance to the X-point region takes the form $J_{\parallel} = \pm k_{\perp} \sigma_{\text{eff}} \Phi$ with effective conductivity $\sigma_{\text{eff}} = (\sigma_{\perp} \sigma_{\parallel})^{1/2}$ (see Ref. 29) where $\sigma_{\parallel} = 2ne^2/m_e v_e$ and $\sigma_{\perp} = \sigma_{\perp\text{pol}}$ or $\sigma_{\perp\text{ve}}$. These models result in a linear boundary condition on J_{\parallel} (i.e. σ_{\perp} independent of Φ), but with an inconvenient non-analytic operator for 2D numerical studies $J_{\parallel} \propto |\nabla_{\perp}|$. Another issue is that for convecting blobs which necessarily require $\partial_t \sim \mathbf{v} \cdot \nabla$, the nonlinear convective term of the polarization drift must be retained. In this case $\sigma_{\perp\text{pol}} = (c^2 \Omega_i / 4\pi v_a^2) (e\Phi/T) (\rho_s / \epsilon_X a_b)^2$ can be used for rough estimates. However, a WKB treatment such as developed in Refs. 28 and 29 cannot be rigorously applied in the presence of nonlinearity. The two-region model considered in this paper circumvents this latter difficulty.

References

- ¹ J. A. Boedo, D. L. Rudakov, R. A. Moyer, *et al.*, Phys. Plasmas **10**, 1670 (2003).
- ² D.L. Rudakov, J.A. Boedo, R.A. Moyer, *et al.*, Nucl. Fusion **45**, 1589 (2005).
- ³ O. Grulke, J.L. Terry, B. LaBombard, and S.J. Zweben, Phys. Plasmas **13**, 012306 (2005).
- ⁴ G. S. Kirnev, V. P. Budaev, S. A. Grashin, E. V. Gerasimov, and L. N. Khimchenko, Plasma Phys. Control. Fusion **46**, 621 (2004).
- ⁵ G. Y. Antar, G. Counsell, J.-W. Ahn, Y. Yang, M. Price, A. Tabasso and A. Kirk, Phys. Plasmas **12**, 032506 (2005).
- ⁶ P. Devynck, P. Ghendrih, Y. Sarazin, Phys. Plasmas **12**, 050702 (2005).
- ⁷ Y.H. Xu, S. Jachmich, R.R. Weynants and the TEXTOR team, Plasma Phys. Control. Fusion **47**, 1841 (2005).
- ⁸ T. A. Carter, Phys. Plasmas **13**, 010701 (2006).
- ⁹ Å. Fredriksen, C. Riccardi, L. Cartegni and H. Pécseli, Plasma Phys. Control. Fusion **45**, 721 (2003).
- ¹⁰ M. Spolaore, V. Antoni, E. Spada, H. Bergsåker, R. Cavazzana, J. R. Drake, E. Martines, G. Regnoli, G. Serianni, and N. Vianello, Phys. Rev. Lett. **93**, 215003 (2004).
- ¹¹ S. J. Zweben, R. J. Maqueda, D. P. Stotler, *et al.*, Nucl. Fusion **44**, 134 (2004).
- ¹² J. L. Terry, S. J. Zweben, K. Hallatschek, *et al.*, Phys. Plasmas **10**, 1739 (2003).
- ¹³ S. I. Krasheninnikov, Phys. Lett. A **283**, 368 (2001).
- ¹⁴ D. A. D'Ippolito, J. R. Myra, and S. I. Krasheninnikov, Phys. Plasmas **9**, 222 (2002).
- ¹⁵ N. Bian, S. Benkadda, J.-V. Paulsen, and O. E. Garcia, Phys. Plasmas **10**, 671 (2003).
- ¹⁶ G. Q. Yu and S. I. Krasheninnikov, Phys. Plasmas **10**, 4413 (2003).

- ¹⁷ D.A. D'Ippolito, J.R. Myra, S.I. Krasheninnikov, G.Q. Yu and A. Yu. Pigarov, *Contrib. Plasma Phys.* **44**, 205 (2004).
- ¹⁸ N. Bisai, A. Das, S. Deshpande, R. Jha, P. Kaw, A. Sen, and R. Singh, *Phys. Plasmas* **12**, 102515 (2005).
- ¹⁹ Y. Sarazin and Ph. Ghendrih, *Phys. Plasmas* **5**, 4214 (1998).
- ²⁰ Ph. Ghendrih, Y. Sarazin, G. Attuel, S. Benkadda, P. Beyer, G. Falchetto, C. Figurella, X. Garbet, V. Grandgirard, and M. Ottaviani, *Nucl. Fusion* **43**, 1013 (2003).
- ²¹ S. Benkadda, P. Beyer, N. Bian, C. Figurella, O. Garcia, X. Garbet, P. Ghendrih, Y. Sarazin and P.H. Diamond, *Nucl. Fusion* **41**, 995 (2001).
- ²² X. Q. Xu, W. M. Nevins, R. H. Cohen, J. R. Myra and P. B. Snyder, *New J. Phys.* **4**, 53 (2002).
- ²³ D. A. Russell, D. A. D'Ippolito, J. R. Myra, W. M. Nevins, and X. Q. Xu, *Phys. Rev. Lett.* **93**, 265001 (2004).
- ²⁴ O.E. Garcia, N.H. Bian, V. Naulin, A.H. Nielsen and J.J. Rasmussen, *Phys. Plasmas* **12**, 090701 (2005).
- ²⁵ M. Umansky, S. I. Krasheninnikov, B. LaBombard, and J. L. Terry, *Phys. Plasmas* **5**, 3373 (1998); B. LaBombard, M. V. Umansky, R. L. Boivin, J. A. Goetz, J. Hughes, B. Lipschultz, D. Mossessian, C. S. Pitcher, J. L. Terry, and Alcator Group, *Nucl. Fusion* **40**, 2041 (2000).
- ²⁶ S.I. Krasheninnikov, D.D. Ryutov, and G.Q. Yu, *J. Plasma Fusion Res.* **6**, 139 (2005).
- ²⁷ G. Q. Yu, S. I. Krasheninnikov and P.N. Guzdar, *Phys. Plasmas* **13**, 042508 (2006).
- ²⁸ J.R. Myra and D. A. D'Ippolito, *Phys. Plasmas* **12**, 092511 (2005).
- ²⁹ D.D. Ryutov and R.H. Cohen, *Contrib. Plasma Phys.* **44**, 168 (2004).
- ³⁰ J.R. Myra, D.A. D'Ippolito, X.Q. Xu and R.H. Cohen, *Phys. Plasmas* **7**, 4622 (2000).
- ³¹ D.A. D'Ippolito and J.R. Myra, *Phys. Plasmas* **13**, 062503 (2006).
- ³² A.V. Nedospasov, V.G. Petrov and G.N. Fidel'man, *Nucl. Fusion* **25**, 21 (1985).

- ³³ J. W. Connor and J. B. Taylor, *Phys. Fluids* **27**, 2676 (1984).
- ³⁴ M. Endler, H. Niedermeyer, L. Giannone, E. Holzhauser, A. Rudyj, G. Theimer, N. Tsois, and the ASDEX Team, *Nucl. Fusion* **35**, 1307 (1995).
- ³⁵ D.A. D'Ippolito and J.R. Myra, *Phys. Plasmas* **10**, 4029 (2003).
- ³⁶ D. Farina, R. Pozzoli and D. D. Ryutov, *Nucl. Fusion* **33**, 1315 (1993).
- ³⁷ M. Ono, M.G. Bell, R.E. Bell *et al.*, *Plasma Phys. Control. Fusion* **45**, A335 (2003).
- ³⁸ E. Marmor, B. Bai, R.L. Boivin *et al.*, *Nucl. Fusion* **43**, 1610 (2003).
- ³⁹ J. R. Myra, D. A. D'Ippolito, D. P. Stotler, S. J. Zweben , R. J. Maqueda, and J. Boedo, "Blob birth and transport in the tokamak edge plasma: analysis of imaging data," submitted to *Phys. Plasmas* (2006).
- ⁴⁰ S. I. Krasheninnikov, A. I. Smolyakov, and T. K. Soboleva, *Phys. Plasmas* **12**, 072502 (2005).
- ⁴¹ H. L. Berk, R.H. Cohen, D.D. Ryutov, Yu. A. Tsidulko and X. Q. Xu, *Nucl. Fusion* **33**, 263 (1993).

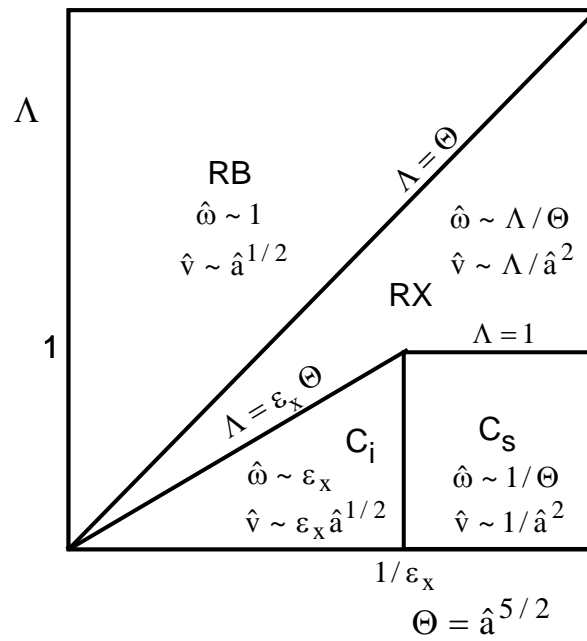


Fig. 1 Regime diagram for the electrostatic two-region model in the space of normalized collisionality Λ , and scale size Θ . In the sheath-interchange (C_s) and ideal-interchange (C_i) regimes the midplane and X-point regions are electrically connected; in the resistive X-point (RX) and resistive ballooning (RB) regimes they are disconnected. Normalized instability growth rates and convective blob velocity scalings are shown for each regime.

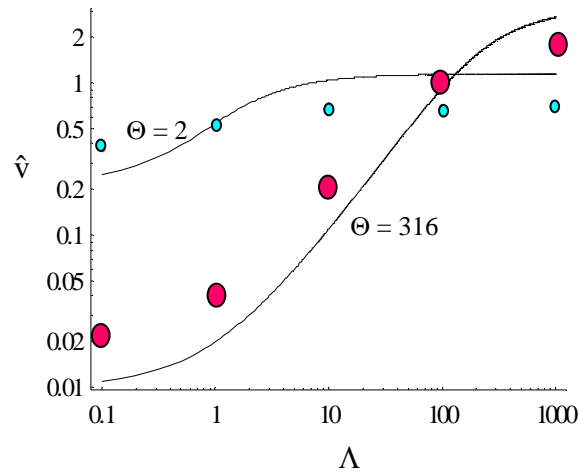


Fig. 2 Normalized radial blob velocity as a function of collisionality parameter Λ for blobs of two different sizes: $\Theta = 2$ ($\hat{a} = 1.3$, small dots) and $\Theta = 316$ ($\hat{a} = 10$, large dots) and $\varepsilon_x = 0.25$. The dots were obtained by measuring the blob velocities from the numerical simulation. The solid curves are from the analytical blob dispersion relation.

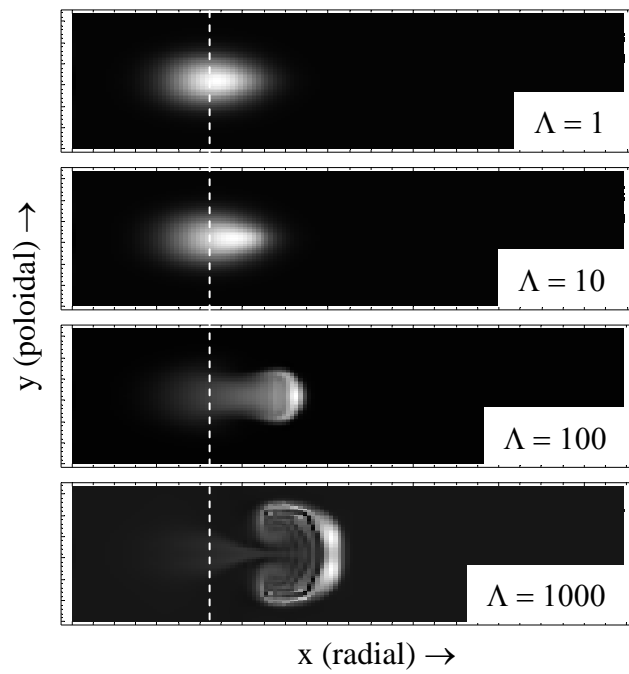


Fig. 3 Snapshot at $\hat{t} = 12.6$ of the density in region 1 from the blob propagation simulations. Results are shown for $\Theta = 316$, $\varepsilon_x = 1/4$ and four different values of Λ . All blobs were centered at the dashed line at $\hat{t} = 0$. Note the different nonlinear evolution and the speeds. .